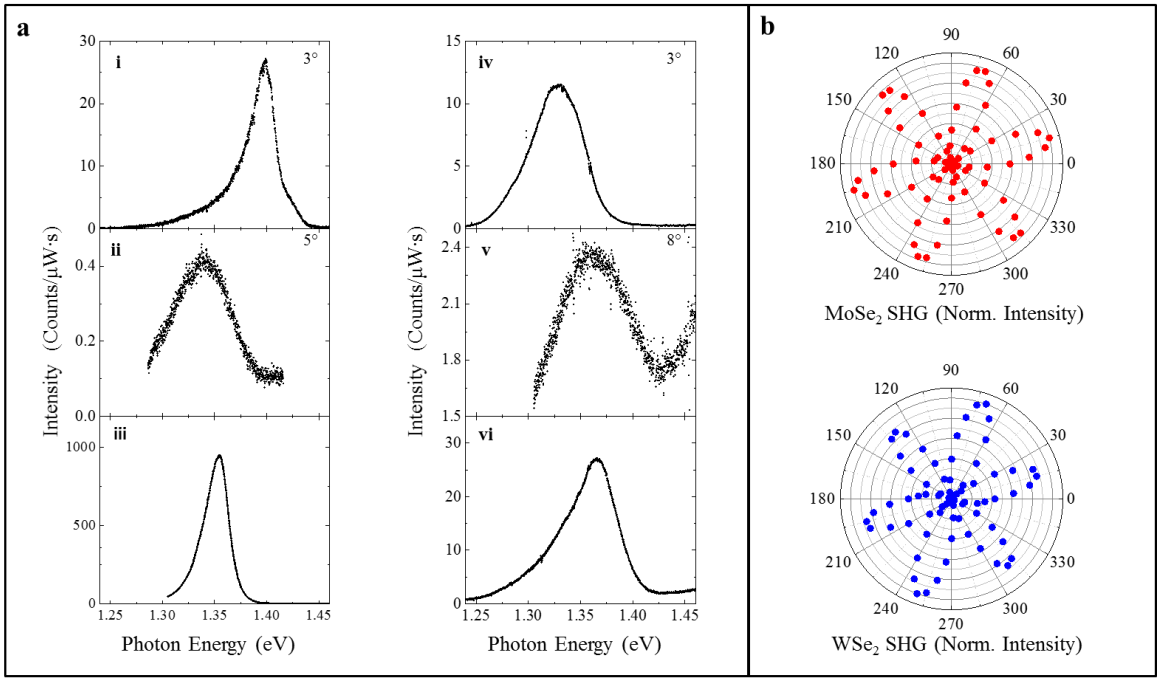

Supplementary Figure 1 | Interlayer exciton PL peak position and heterostructure twisting angle. a, Photoluminescence from the interlayer exciton for six WSe_2-$MoSe_2$ heterostructures under cw laser excitation at 1.96 eV. The peak position of each heterostructure is influenced by several factors, including the interlayer separation and interlayer exciton density under photoexcitation. Interlayer spacing affects the binding energy of the interlayer exciton, while interlayer exciton density affects the PL energy as a result of dipole-dipole interactions. **b,** Polarization resolved second harmonic generation in resonance with the intralayer exciton of isolated monolayer $MoSe_2$ and WSe_2 from **i**, which is Device 1 from the main text. We employ polarization resolved second harmonic generation (SHG) for crystal axis determination of individual monolayers[1]. The twisting angle, or difference between the crystal axes of the constituent layers of the HS, is inset for those HS where it is possible to discern the angle. For HS **i** and **v**, the twisting angle is found from the angular difference between isolated monolayer regions that compose the HS. However, not all devices have isolated monolayers, as they are often covered during the transfer step in the fabrication procedure. Thus, we employ SHG on the attached bulk from which monolayer $MoSe_2$ or WSe_2 was exfoliated to determine the angular difference for HS **ii** and **iii**. For samples **v** and **vi** a single layer completely overlaps an isolated second layer, making the twisting angle indiscernible with this technique. We observe bright interlayer exciton for twisting angles up to 8°. We are unable to conclude any role of the twisting angle from the small sample size used in this report. However, we expect future studies more focused on the stacking orientation of constituent layers to expose the influence of the twisting angle on the properties of the WSe_2-$MoSe_2$ heterostructure and interlayer exciton.

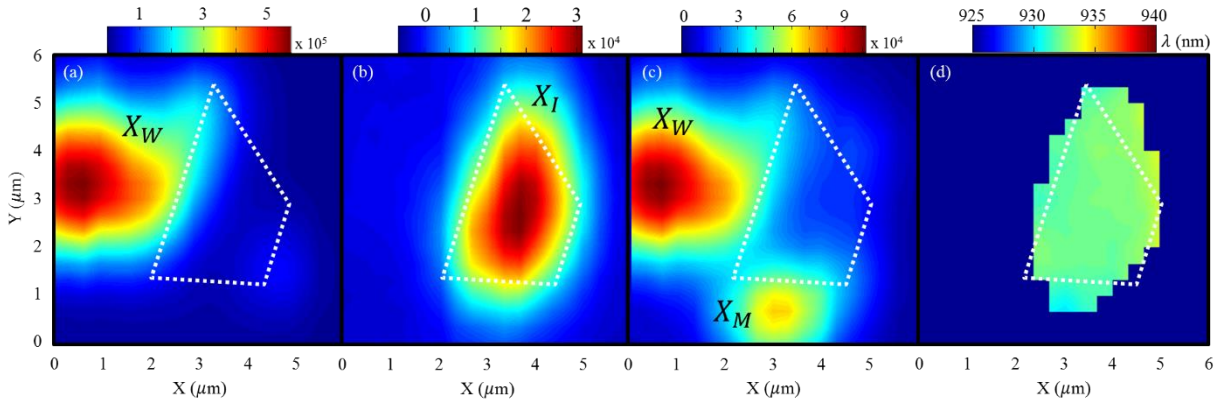

Supplementary Figure 2 | Two-dimensional spatial maps of spectrally integrated PL from Device 1. Spatial maps of the spectrally integrated intensity at room temperature from **a,** intralayer excitons in monolayer WSe_2 (X_W), **b,** interlayer excitons in the $MoSe_2$-WSe_2 heterostructure (X_I), and **c,** intralayer excitons in monolayer $MoSe_2$ (X_M). The dashed white line corresponds to the $MoSe_2$-WSe_2 heterostructure region shown in Figure 1b of the main text. Note that the intensity of X_W dominates that of X_M, preventing its complete spatial isolation. Accordingly, Supplementary Figure 2c includes X_W on the left hand side of the outlined HS region, just as in Supplementary Figure 2a. **d,** Spatial dependence of the center of a Gaussian fit to X_I, with spectra at the background threshold appearing dark blue. Importantly, X_I extends across the entire HS region, but does not appear elsewhere. The uniform spatial and spectral isolation of X_I to the heterostructure region strongly suggest that its origin is not from defect related excitons. Spatial maps were taken at room temperature after 13 thermal cycles from room temperature to 30K or lower.

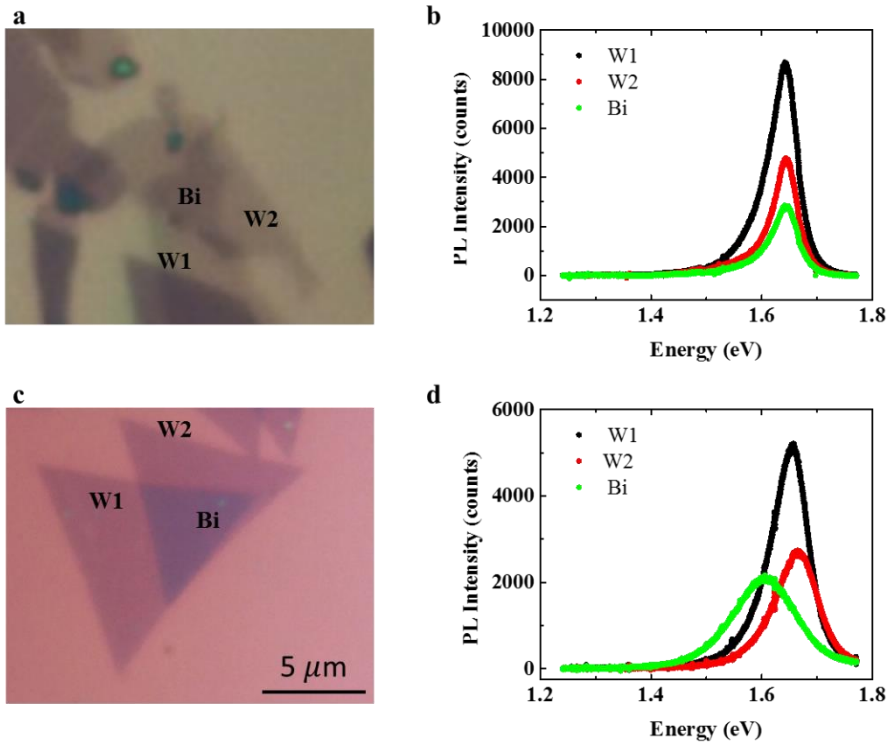

Supplementary Figure 3 | Homobilayer WSe_2 photoluminescence. Microscope image of a vertically stacked WSe_2-WSe_2 homostructure from **a**, exfoliated and **c**, physical vapor transport (PVD) grown WSe_2, with monolayer regions (W1, W2), and bilayer region (Bi) labeled. Photoluminescence spectra of the individual monolayers and the vertically stacked bilayer region from **b**, exfoliated and **d**, PVD WSe_2-WSe_2 homostructure. Notably, there is no low energy photoluminescence that would suggest the presence of interlayer exciton.

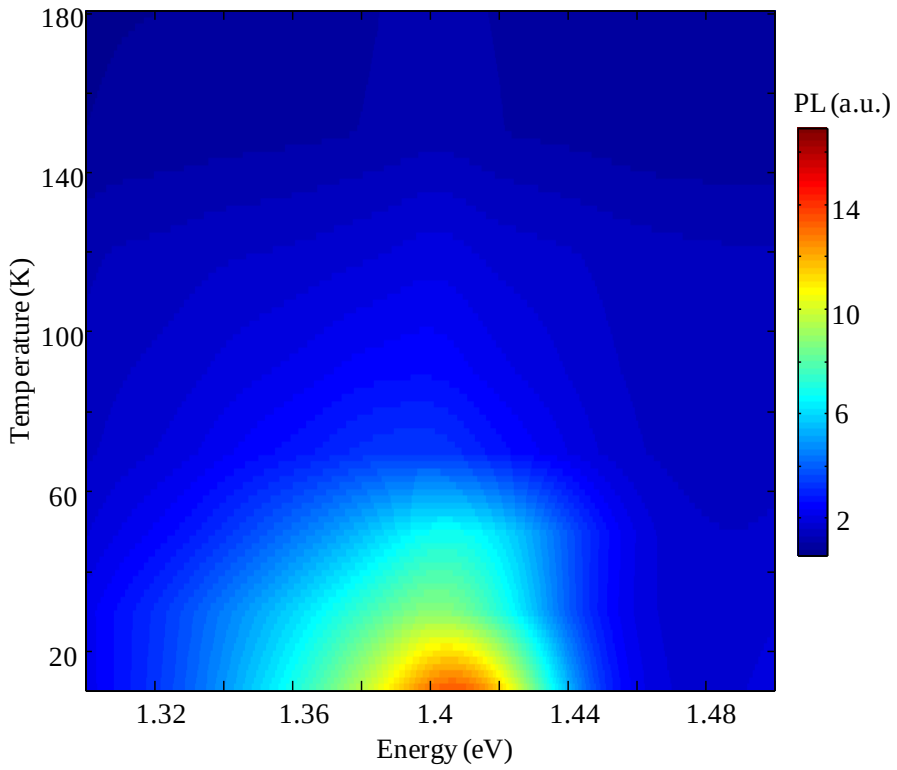

Supplementary Figure 4 | Temperature dependence of interlayer exciton.
Photoluminescence intensity plot showing decreasing PL intensity of the interlayer exciton with increasing temperatures.

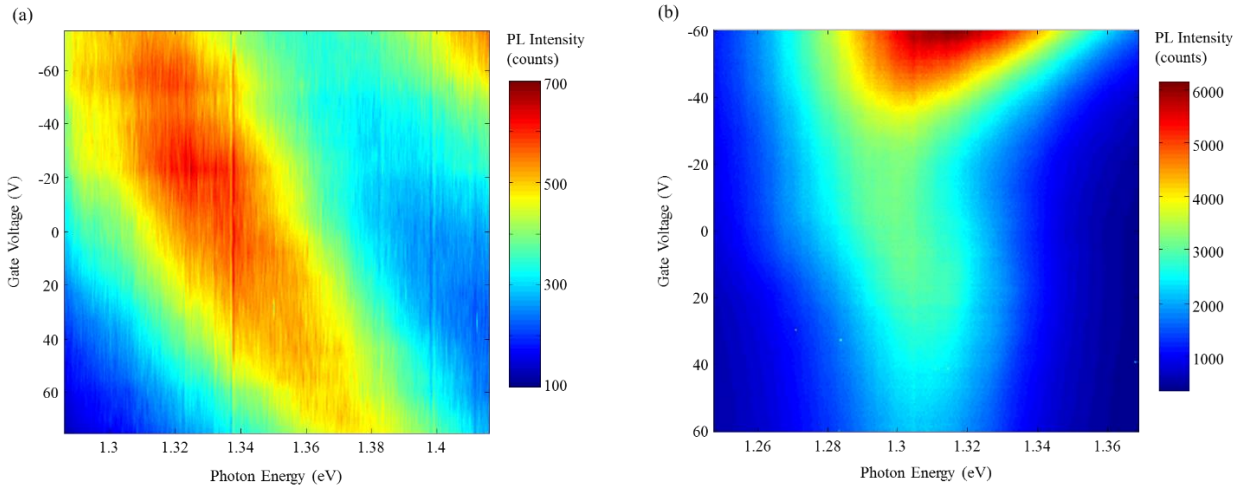

Supplementary Figure 5 | Electrical control of interlayer exciton. a, Color map of interlayer exciton photoluminescence from Device 3, as a function of applied gate voltage. Here, the $MoSe_2$ monolayer is stacked on top of the WSe_2, which is an inverted analogue of Device 2. Since the interlayer exciton dipole is oriented in the direction from $MoSe_2$ to WSe_2, this device architecture results in a dipole direction exactly opposite that of Device 2 (Figure 3c in main text). In this case, the coupling of the field to the spatially indirect exciton results in the reverse exciton energy shift under an applied gate voltage. Therefore, the red shift of the interlayer exciton in this architecture is a consequence of the inverted permanent dipole compared to Device 2. Combined with Figure 3c and Supplementary Figure 5b, the observed red shift of nearly 60 meV from this device clearly demonstrates the direction of the interlayer exciton electric dipole moment, it's coupling to the field, and the direct electrical control of the heterostructure band-offset. Note that the encroaching signal with energy greater than 1.4 eV at high negative gate is due to the low energy tail of the $MoSe_2$, which has enhanced intensity at this doping level. **b**, Photoluminescence intensity plot of interlayer exciton of an additional device with WSe_2 on top of $MoSe_2$.

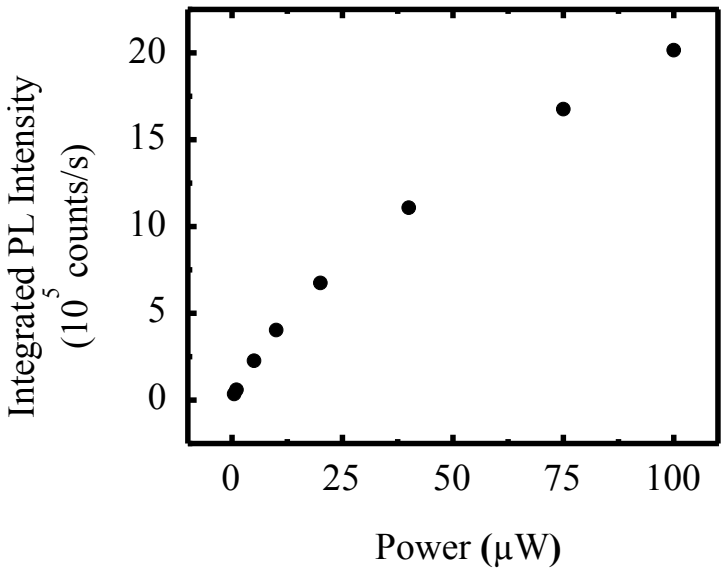

Supplementary Figure 6 | Power saturation threshold for interlayer exciton photoluminescence. Interlayer exciton photoluminescence as a function of excitation power with laser in resonance with the intralayer exciton of WSe_2 (1.722 eV). The interlayer exciton photoluminescence shows sublinear power response even for the lowest excitation power of 0.5 μW.

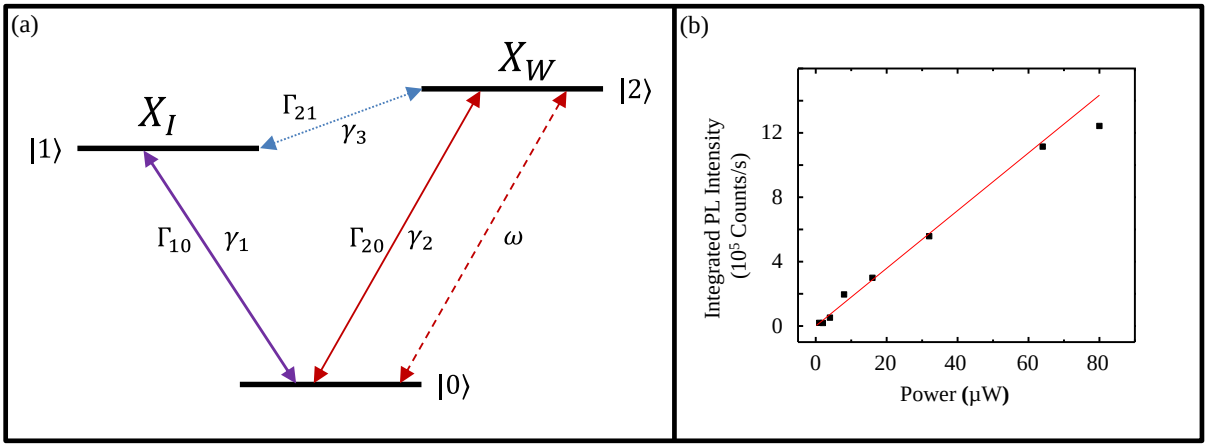

Supplementary Figure 7 | Power saturation of interlayer exciton photoluminescence. a, 3-Level V energy diagram for the relaxation of intralayer excitons in WSe_2 (X_W) to interlayer excitons (X_I) at the WSe_2-$MoSe_2$ heterojunction. Γ denotes the relaxation rates, and γ the dephasing rates, for each transition. The excitation laser (ω) is in resonance with the optical dipole transition $|0\rangle \Leftrightarrow |2\rangle$. **b,** Power dependence of the X_W emission on the heterostructure region. The linear fit, in red, reveals a power saturation threshold of about 80 μW.

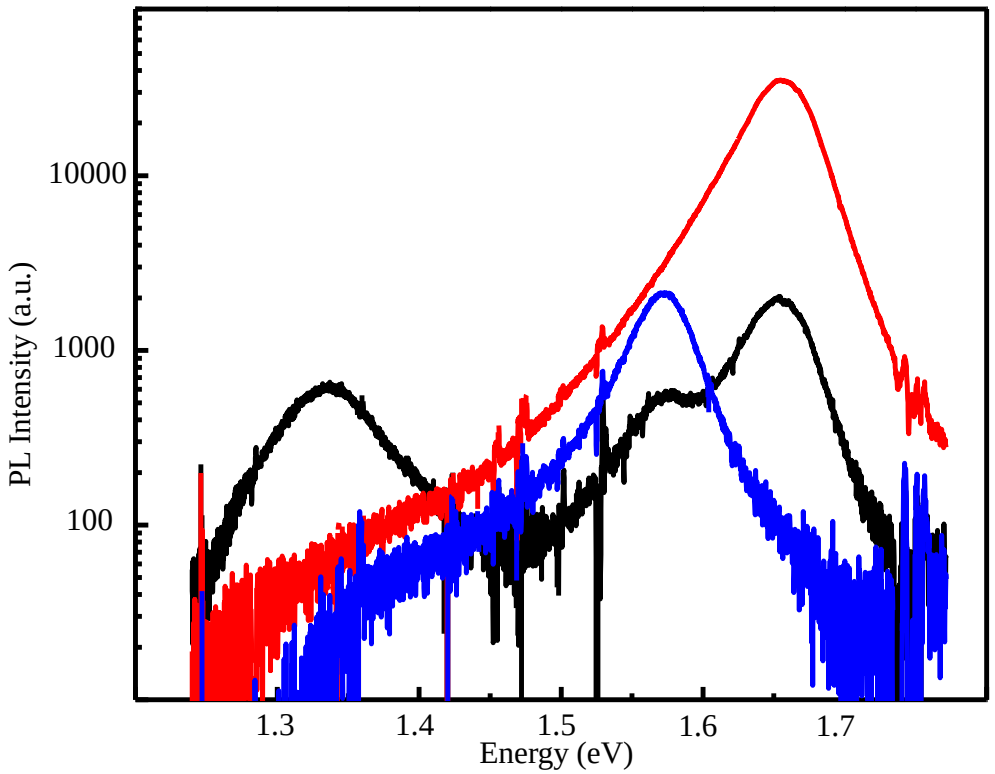

Supplementary Figure 8 | Room temperature photoluminescence. Photoluminescence from individual monolayers of WSe_2 (red) and $MoSe_2$ (blue) are quenched by an order of magnitude on the heterostructure (black). Data are taken from device 1 after a thermal cycle. These PL measurements show that the intralayer exciton emission at the heterostructure region is quenched compared to isolated monolayers. This observation implies that interlayer charge transfer is fast compared to the intralayer exciton recombination rate. Importantly, there is a distinct difference in the quenching ratio at room temperature and low temperature. At room temperature, the PL of intralayer excitons X_{Mo} and X_W is quenched by at least an order of magnitude (Supplementary Figure 8), while at low temperature the intralayer exciton PL is only slightly quenched (Figure 1d). This implies that the interlayer carrier hopping rate strongly depends on the temperature and is reduced at lower temperature. Moreover, at low temperature (20 K), we find the spectrally integrated exciton PL intensity is conserved between isolated monolayers and the heterojunction, while at room temperature the integrated PL intensity from the heterojunction is an order of magnitude smaller than the summation of isolated monolayers. This observation implies that at low temperature the quenched population of intralayer excitons is transferred to form interlayer excitons, which then relax mainly via radiative recombination. In contrast, at room temperature, a non-radiative relaxation channel dominates the interlayer exciton relaxation, giving rise to the quenching of the spectrally integrated heterojunction PL intensity.

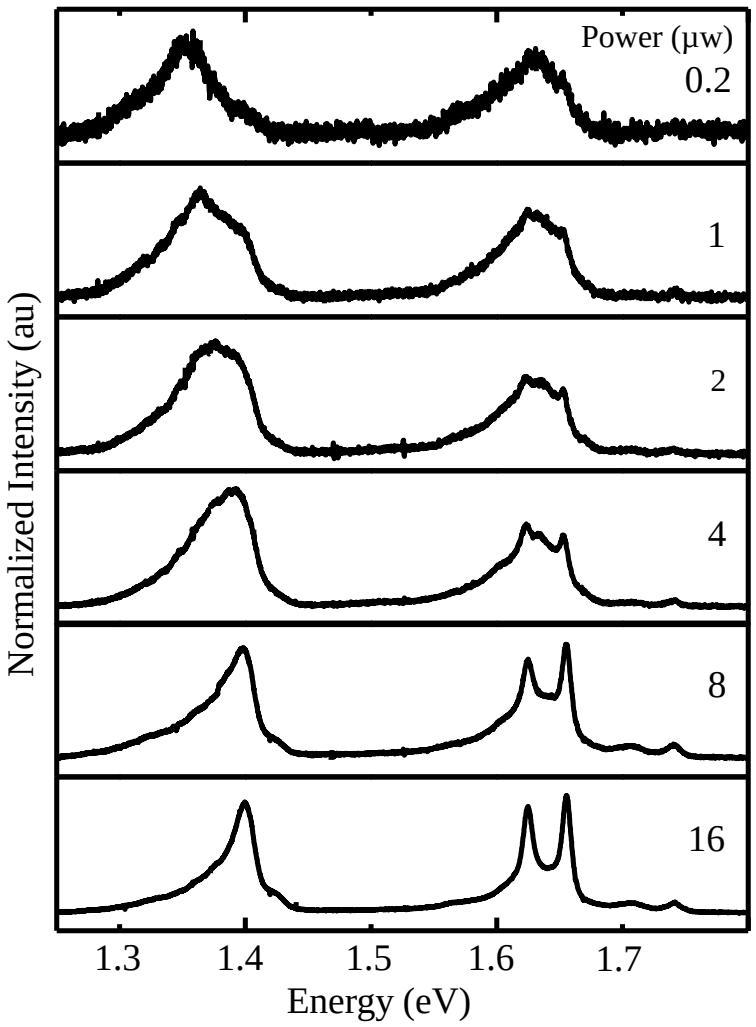

Supplementary Figure 9 | Power dependence of interlayer exciton photoluminescence. Photoluminescence intensity as a function of power for the heterostructure region of device 1, normalized to the peak intensity. Experimental temperature is 20 K and the excitation energy is 1.88 eV. The interlayer peak is composed of a doublet corresponding to the $MoSe_2$ conduction band splitting.

Supplementary Discussion

To understand the low power saturation threshold of the interlayer exciton in the PLE results (Figure 4b), we consider the simplest three-level V diagram model. As shown in Supplementary Figure 7, state $|2\rangle$ represents intralayer excitons in the WSe_2 monolayer (X_W), state $|1\rangle$ represents interlayer excitons (X_I), and $|0\rangle$ represents the ground state of the system (no exciton), Γ denotes the relaxation rates, and γ denotes the dephasing rates for each transition. Monochromatic CW laser excitation couples the driving field (ω) to the optical dipole ($\mu_{20} = \mu_{02}$) for the transition $|0\rangle \Leftrightarrow |2\rangle$. In this simplified model, we assume that the interlayer charge transfer rate is ultrafast compared to the radiative relaxation rates, such that $\Gamma_{21} \gg \Gamma_{20}, \Gamma_{10}$.

The hamiltonian for the three-level V system above, taking the rotating wave approximation in the Schrödinger representation, is given by $H = \hbar \begin{bmatrix} 0 & 0 & \chi_{02}^* \\ 0 & \omega_{10} & 0 \\ \chi_{20} & 0 & \omega_{20} \end{bmatrix}$ with $\chi_{02} = \overrightarrow{\boldsymbol{\mu_{02}}} \cdot \vec{\mathbf{E}}\, e^{-i\omega t}$, with $\hbar\omega_{i0}$ being the energy of ith radiative decay. We treat the density matrix for the system according to the Schrödinger equation:

$$\frac{d\rho}{dt} = -\frac{i}{\hbar}[H, \rho] + Decay + Dephasing$$

$$Decay = \begin{bmatrix} \rho_{11}\Gamma_{10} + \rho_{22}\Gamma_{20} & 0 & 0 \\ 0 & \rho_{22}\Gamma_{21} - \rho_{11}\Gamma_{10} & 0 \\ 0 & 0 & -\rho_{22}(\Gamma_{20} + \Gamma_{21}) \end{bmatrix}$$

$$Dephasing = \begin{bmatrix} 0 & -\rho_{01}\gamma_1 & -\rho_{02}\gamma_2 \\ -\rho_{10}\gamma_1 & 0 & -\rho_{12}\gamma_3 \\ -\rho_{20}\gamma_2 & -\rho_{21}\gamma_3 & 0 \end{bmatrix}$$

Taking the steady-state approximation ($\dot{n_\iota} \equiv \dot{\rho_{\iota\iota}} = 0$) and assuming conservation of population yields the rate equations

$$n_1 \Gamma_{10} + n_2 \Gamma_{20} + \alpha(n_2 - n_0) = 0$$

$$n_2(\Gamma_{20} + \Gamma_{21}) + \alpha(n_2 - n_0) = 0$$

$$n_0 + n_1 + n_2 = 1$$

where $\alpha \equiv 2\frac{|\chi_{20}|^2 \gamma_2}{\gamma_2^2 + \delta^2}$ and $\delta \equiv \omega_{20} - \omega$ The off-diagonal matrix element can then be written as

$$\rho_{20} = \frac{\chi_{20}}{(\gamma_2^2 + \delta^2)(1 + \alpha\beta)}(i\gamma_2 - \delta), \qquad \beta = \frac{(2\Gamma_{10} + \Gamma_{21})}{\Gamma_{10}(\Gamma_{20} + \Gamma_{21})}$$

The absorption of the μ_{20} dipole is given by the imaginary part of ρ_{20}:

$$Absorption \propto Im\{\rho_{20}\} = \frac{\chi_{20}\gamma_2}{(\gamma_2^2+\delta^2)(1+\alpha\beta)} = \frac{\chi_{20}\gamma_2}{\delta^2+\gamma_2^2\left(1+\frac{2(2\Gamma_{10}+\Gamma_{21})|\chi_{20}|^2}{\Gamma_{10}(\Gamma_{20}+\Gamma_{21})\gamma_2}\right)}$$

The absorption has Lorentzian dependence, and the saturation intensity for the interlayer exciton, $I_{S(X_I)}$, can be found,

$$\frac{I}{I_{S(X_I)}} = \frac{2(2\,\Gamma_{10}+\,\Gamma_{21})|\chi_{20}|^2}{\Gamma_{10}(\,\Gamma_{20}+\,\Gamma_{21})\gamma_2} \Rightarrow \frac{2|\chi_{20}|^2}{\Gamma_{10}\gamma_2} \quad ; \quad [\,\Gamma_{21} \gg \Gamma_{20}\,]$$

$$I_{S(X_I)} = I\,\frac{\Gamma_{10}\gamma_2}{2|\chi_{20}|^2} = \frac{\tau_{X_W}}{\tau_{X_I}} I_{S(X_W)}$$

where $I_{S(X_W)} = \frac{\hbar^2\,\Gamma_{20}\gamma_2}{2|\mu_{20}|^2}$ is the saturation intensity for an intralayer exciton in an isolated WSe_2 and $\tau_{ij} = \frac{1}{\Gamma_{ij}}$. We can see that the saturation intensity of interlayer exciton can be extremely small compared to intralayer exciton if its life time is much longer than that of intralayer ones. Using experimentally determined parameters $\tau_{X_W} \simeq 10$ ps,[2] $\tau_{X_I} = 1.8$ ns we calculate that the power saturation threshold of X_I is about 180 times smaller than that of X_w. This simplifed model predicts a power saturation threshold of $\simeq$ 0.5 μW for X_I, which is consistent with the experimental observation.

Supplementary References

1 Hsu, W. T. *et al.* Second harmonic generation from artificially stacked transition metal dichalcogenide twisted bilayers. *ACS Nano* **8**, 2951-2958, doi:10.1021/nn500228r (2014).

2 Wang, G. *et al.* Valley dynamics probed through charged and neutral exciton emission in monolayer WSe2. *Physical Review B* **90**, 075413 (2014).